Spring 2021

A Karst Feature Prediction Model For Prince Of Wales Island, Alaska Based On High Resolution Lidar Imagery

Alexander Lyles
Fort Hays State University, aslyles@mail.fhsu.edu

A KARST FEATURE PREDICTION MODEL FOR

PRINCE OF WALES ISLAND, ALASKA BASED

ON HIGH RESOLUTION LiDAR IMAGERY

being

A Thesis Presented to the Graduate Faculty

of Fort Hays State University in

Partial Fulfillment of the Requirements for

The Degree of Master of Science

by

Alex Lyles

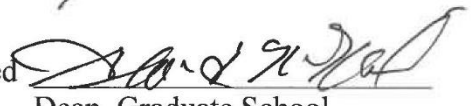B.S. Geology, Ohio University

Date __4-26-21__

Approved _____
Major Professor

Approved _____
Dean, Graduate School

This thesis for
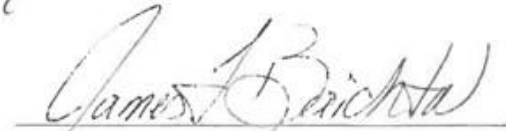
the Master of Science Degree
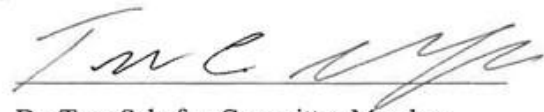
by

Alexander S. Lyles

has been approved

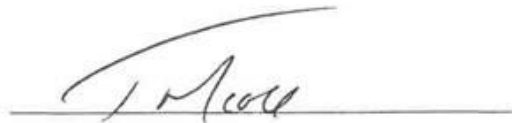Dr. Jonathan Sumrall, Committee Chair

Dr. James Baichtal, Committee Member

Dr. Tom Schafer, Committee Member

Dr. Richard Lisichenko, Committee Member

Dr. Todd Moore, Chair, Dept. of Geosciences

ABSTRACT

Investigation into surface karst formation is significant to hazard prediction, hydrogeologic drainage, and land management. Southeast Alaska contains over 600,000 acres of mapped carbonate bedrock, and some of the fastest recorded karst dissolution in the world. The objectives of this study are to develop and compare multiple semi-automated models to map and delineate karst features from bare-earth LiDAR imagery using ArcGIS Desktop 10.7, and to apply a preliminary geostatistical analysis of sinkhole morphometric parameters to highlight potential spatial patterns of karst evolution on Prince of Wales Island, Alaska. A semi-automated approach of mapping karst features provides a dataset that minimizes error from noise while maintaining accurate depression location and catchment boundaries. Several semi-automated models with different size parameters were compared against field-validated data using vulnerability as a proxy to determine the most accurate size threshold model. The model with the most overlap agreement was used to determine the morphometrics of karst features identified. This study conducted preliminary analysis of morphometric properties derived from the semi-automated karst feature prediction model to provide context for the geologic controls that allow for such large, rapid karstification observed in the region. Although beyond the scope of this study, morphometric analysis utilizing this semi-automated approach should be the focus of future studies to determine formation mechanisms and factors of karst landscape evolution through time.

ACKNOWLEDGMENTS

This thesis is dedicated to Jim Nieland.

This thesis would not have been possible without the support of numerous individuals throughout my time in graduate school, some of whom may not be mentioned by name.

Foremost, I would like to thank my advisor, Dr. Jon Sumrall, for his patience, motivation, enthusiasm, and immense knowledge. Jon's support of my decisions and guidance throughout the research process is the reason this thesis fully came to fruition and I cannot imagine having a better advisor during my master's study.

Besides my advisor, I would like to thank the rest of my committee: Dr. Richard Lisichenko, Dr. Tom Schafer, and Dr. Jim Baichtal for their insight, encouragement, and difficult questions. I want to thank Jim specifically for his ability to inspire passion in science and for awakening my love of soft rocks, karst, and fine scotch.

My sincere thanks also go out to the Sitka Conservation Society and the Tongass National Forest for providing the support to expand this study to a much larger area than would have otherwise been possible.

I want to acknowledge my friends that have stuck by my side up to and during the interesting year of 2020: Tyler Shockey, Tristan Cormack, Nils Illokken, Ben McIntosh, Nick Kirwen, Matt Watts, Ed Guisinger, Anthony Jameson, Kat Meitner, Mitch Lukens, and others. I also want to thank Anna Harris for her positivity, support, friendship, and co-development as a karst scientist.

Lastly, I want to thank my family for their undying belief in me. None of this would have been possible without their strong mental, emotional, and practical support.

TABLE OF CONTENTS

LIST OF FIGURES

LIST OF EQUATIONS

Equation
Number

LIST OF TABLES

1.0 INTRODUCTION

Southeast Alaska experiences the fastest recorded karst dissolution and stream

downcutting in the world (Allred, 2004; White, 2007). The potential to effectively map,

delineate, and predict karst features and hazards in southeast Alaska offers benefit to

industrial, recreation, and conservation efforts in the region. The densely forested karst

landscapes of southeast Alaska comprise systems with complexities stemming from a

long tectonic and glacial history. An automated karst feature model that predicts locations

and delineates highly vulnerable karst is a large step in the right direction with regards to

recognizing the complex hydrology tied to karst landscapes in Alaska. Much of the

research into karst formation in the region stems from efforts to properly understand and

manage the important resources associated with karst lands (Baichtal and Swanston,

1996; Bachtal, 1997; Bryant et al., 1998; Baichtal and Langendoen, 2001; Curry, 2003;

McClellan et al., 2003; Langendoen and Baichtal, 2004; Prussian and Baichtal, 2004;

Kovarik et al., 2005; Hendrickson, 2006; Kovarik, 2007; Hendrickson and Groves, 2011;

Kovarik, 2013; Kovarik, 2013; Kovarik and Baichtal, 2016; Harris, 2020). The use of

sub-meter resolution Light Detection and Ranging (LiDAR) bare-earth imagery by the

US Forest Service and US Geological Survey has revealed the karst topography of the

Prince of Wales Island area in high detail (DGGS, 2013). This bare-earth dataset is

reconditioned in this study to delineate and incorporate karst features into a GIS database.

These polygon features are also analyzed using geographical statistics of spatial

parameters to assess trends in the geomorphological properties. Southeast Alaska consists

of a large group of islands known as the Alexander Archipelago, as well as the coastal

strip of mainland that shares a border with Canada to the east. Most of the islands are

contained between 55° and 60° north latitude, stretching ~120 miles in width and ~525 miles in length in the northwesterly-southeasterly direction (Figure 1). The Alexander Archipelago comprises hundreds of islands with nearly 10,000 miles of mostly rocky, steep coastline (Harris et al., 1974). Prince of Wales Island is the largest island in the archipelago with an area of ~2,770 square miles and ~990 miles of coastline (Figure 1). Due to the extensive logging history on the island, over 1,500 miles of roads connect many parts of the island and allow access to otherwise extremely remote areas.
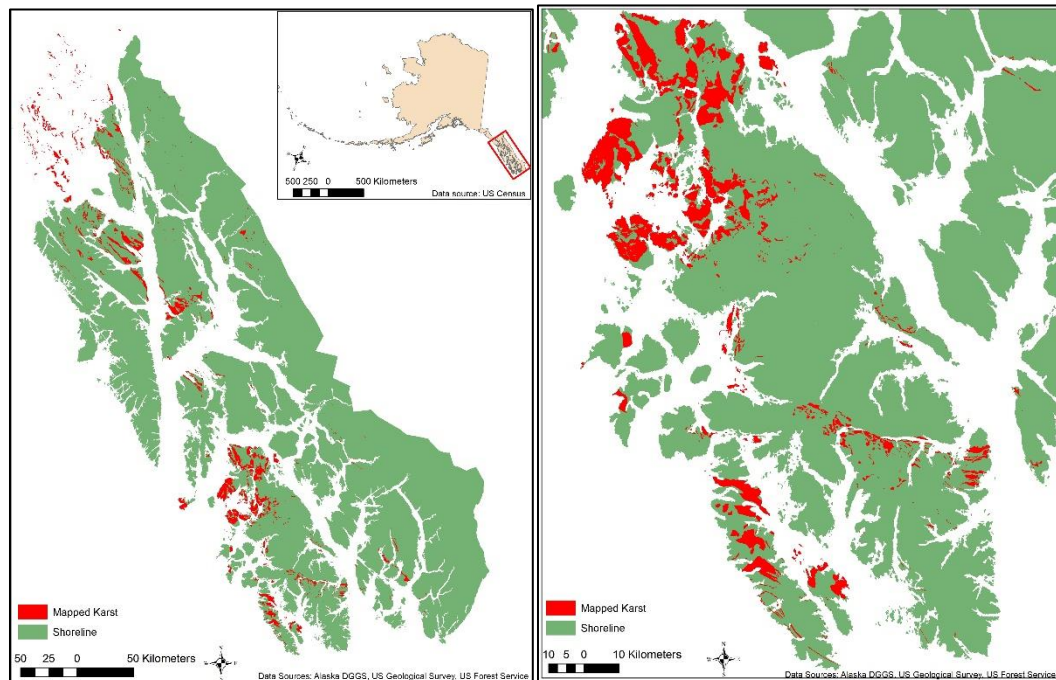
Figure 1. Mapped Carbonate Bedrock (Red) in Southeast Alaska (Left) and the Prince of Wales Island Area (Right).

The karst in the region is considered glaciokarst, a specific type of landscape with peculiarities stemming from diverse weathering effects such as glacial and fluvial erosion, frost weathering, and mass movements of sediment on soluble bedrock (Veress et al., 2019). Karst features present an excellent model for understanding current and past

climatic changes and the effects these fluctuations have on landscapes (Veress et al., 2019). Prince of Wales Island contains structurally complex geology and has been heavily impacted by past ice flows due to the Cordilleran Ice Sheet (CIS) that covered most of the region with ~3,000 feet of ice during the Wisconsin Glaciation (Harris et al., 1974; Kienholz et al., 2015; Lesnek et al., 2020). The morphological parameters used for analysis of surface karst landscape features include circularity index, azimuth of long and short axes, elongation ratio, and area of feature (Day, 1983; Basso et al, 2013; Kobal et al., 2015). Patterns and correlations in these parameters offer insight into the dominant geologic controls of karstification on the landscape, as well as assist in prediction of future geologic hazards.

This study seeks to: 1) develop a semi-automated, vector-based karst feature prediction model to accurately map and delineate surface karst features from high resolution bare-earth LiDAR imagery, 2) determine the level of overlap for the karst feature prediction model using a comparison of delimited areas recently field-surveyed for karst depressions, and 3) derive morphometric characteristics of surface karst features. A semi-automated approach of mapping karst features provides a dataset that minimizes error from noise while maintaining accurate depression location and catchment boundaries. A comparison of overlap is made between the extensive polygon dataset created by the karst feature prediction model developed during this study and areas recently field-surveyed for karst vulnerability. Morphometric parameters of surface karst features, such as circularity index and sinkhole long axis orientation, extracted during this study, will show statistical variation through preliminary analysis and encourage further research into the geomorphology of the region.

2.0 REVIEW OF THE LITERATURE

2.1 Karst Processes

Karstification is a continuous process where acidic water dissolves soluble bedrock to create subsurface hydrologic networks (White, 1988; Ford and Williams, 2007; Palmer, 2007). Karst is a geomorphologic term that can be defined as a terrain with distinct hydrology and landforms that result from a combination of high rock solubility and well-developed secondary porosity (White, 1988; Ford and Williams, 2007; Palmer, 2007). Carbonate and evaporite lithologies displaying some karst terrain formation occur over ~20% of Earth's ice-free surface and provide drinking water for ~25% of Earth's population (White, 1988; Ford and Williams, 2007; Palmer, 2007). Karst groundwater circulation occurs when there are established connections between recharge points and subterranean conduits (White, 1988; Ford and Williams, 2007; Palmer, 2007). While rock solubility is important in karst formation, high solubility alone is not enough to produce a karst landscape that can sustain an evolving subsurface conduit system (White, 1988; Ford and Williams, 2007; Palmer, 2007). The ideal lithology to form classic karst is dense, massive carbonate rock with a pure chemical composition and a coarse fracture pattern to allow water to permeate through the rock, creating corrosive voids (White, 1988; Ford and Williams, 2007; Palmer, 2007). A high primary porosity in highly soluble rocks often results in poorly formed karst, as the dissolution potential of corrosive water is expended near the surface instead of preferentially in subsurface voids (White, 1988; Ford and Williams, 2007; Palmer, 2007). A dense and highly soluble rock with low primary porosity and mature secondary, or fracture, porosity will result in a more stable

4

karst system capable of evolving and enlarging over time (Figure 2) (Ford and Williams, 2007; Audrey and Palmer, 2015).
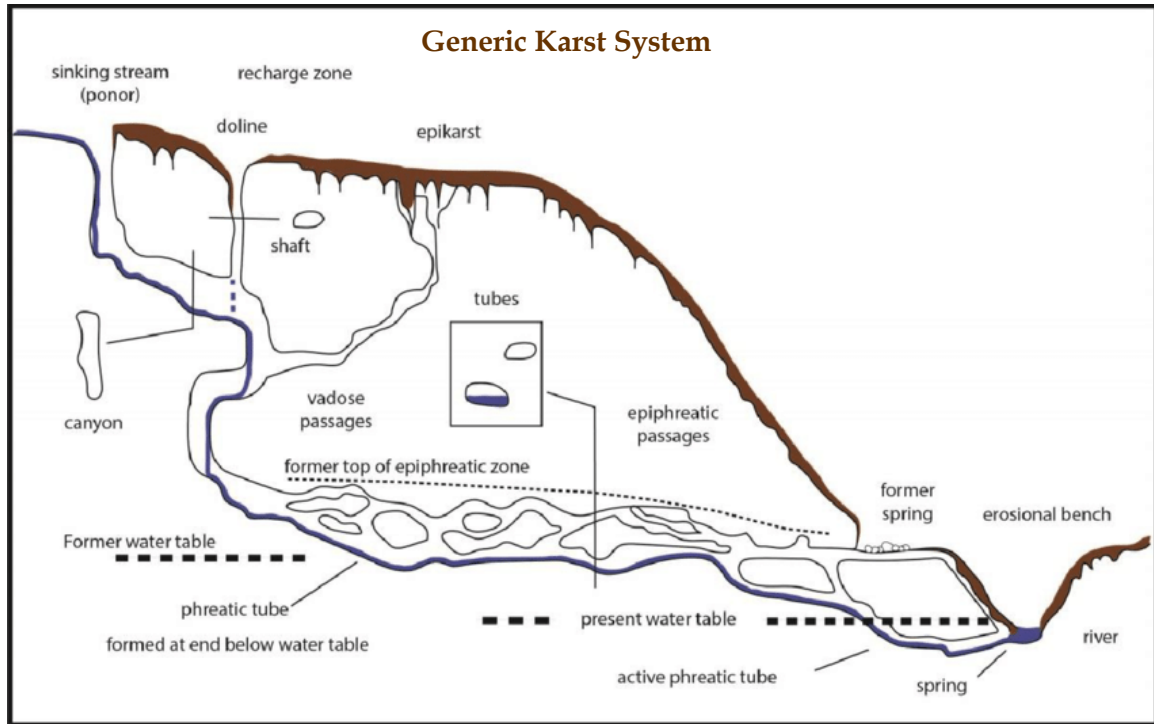
Figure 2. Idealized cross-section of a typical epigenic karst system (Modified from Audra and Palmer, 2015).

Karst can be viewed as an open system comprising two integrated geochemical and hydrological components that act upon the rocks: endokarst and exokarst. The subsystems can be split between karst features that form above (exokarst) and below (endokarst) the exposed landscape surface (Ford and Williams, 2007). Exokarst forms primarily through direct precipitation and includes sinkholes, grikes, losing streams, and karren (Figures 2 and 3) (Williams, 2008). Endokarst refers to underground karst, or the conduits and voids that form via corrosion of subsurface soluble rock (Figure 2) (Bogli, 2012). Exokarst features best form in areas of high precipitation acting on crystalline carbonate lithology that lies above the water table and contains low primary porosity (Williams, 2008). Epikarst, also known as the subcutaneous zone, falls into the exokarst

subcategory and is composed of weathered bedrock that is exposed at the surface or immediately beneath soil, if present (Figure 3). Well-formed epikarst lies in the vadose zone above the water table and is dominated by transmission rather than storage but contains a suspended aquifer that slowly percolates water downward, sustaining distal tributaries of caves and perennial springs (Williams, 2008). The preferential pathways for water circulation in vadose zones of structurally complex karst areas are folded bedded interfaces, while fracture clusters provide through connectivity for water conduits (Antonellini et al., 2019). The combination of fracture clusters and continuous water flow leads to roof collapse, resulting in large cave chambers or sinkholes (Antonellini et al., 2019). Since both the surface landscape and subterranean conduits of karst systems evolve simultaneously, to understand karst hydrogeology, it is also necessary to understand karst geomorphology, and vice versa (Ford and Williams, 2007).

Figure 3. Well-Developed Epikarst on Dall Island, Alaska Showing Intense Nature of Surface Dissolution. (Credit: Jim Baichtal)

2.2 Geospatial Analysis of Karst Landscapes

Geographic Information Systems (GIS) produce layered visual and data outputs

using spatial and attribute data, GIS software, and tools for modeling and analysis

(Maguire, 1991; Farkas et al., 2016). This study utilized a Digital Terrain Model (DTM),

a specific type of Digital Elevation Model (DEM), created directly from a LiDAR point

cloud using only the last return, or ground points, of the elevation dataset. The conversion

of generic DEM into a DTM removes nearly all vegetation cover and artificial structures

and is vital for the analysis of geologic landforms in densely forested areas (Kobal et al,

2015). Digital models of elevation surfaces comprise extremely large numbers of records

that represent measurements or estimations of the elevation at various points in space,

meaning that there is inherent error and uncertainty tied to the continuous dataset as a

whole (Fisher and Tate, 2006). False depressions historically result from data noise,

interpolation error, and limited resolution of DEM datasets and need to be removed to

conduct hydrogeographical analysis (Lindsey and Creed, 2006). For this study, DTM and

DEM are used interchangeably and refer to the same bare-earth data.

Depressions in karst, also known as sinkholes, dolines, sinks, basins, or pits, are

local minimums that have no downslope flow paths to any adjacent cells in a DEM. A

semi-automated method of karst landscape analysis in GIS has been developed using the

Hydrology Fill Tool in ArcGIS Desktop (Doctor and Young, 2013). The Fill Tool in

ArcMap 10.7 uses the priority-flood algorithm, which originated as a tool to remove

"error", or areas where streams would intersect closed depressions, creating disjointed

hydrological networks from DEMs in non-karst areas (Wang and Liu, 2006). The sink-fill

function subtracts the original DTM from the Fill Tool outcome using Raster Calculator

in ArcMap 10.7 to show depth below spill-level of the closed depressions that characterize karst topography (Doctor and Young, 2013). This function is important for analysis in zones of thick deposits of carbonate bedrock because it indicates where water is entering the subsurface. However, as the resolution of DTMs increase, more hydrologic sinks are created in error due to falsely identified closed depressions. The major difficulty in a semi-automated approach to karst surface mapping stems from the need to reduce the number of depressions created from the sink-fill method to better represent the actual surface hydrology (Doctor and Young, 2013; Zumpano et al., 2019). This includes manually removing falsely identified depressions created from road quarries and streams intersecting roadways, which appear as dams without specific raster reconditioning (Doctor and Young, 2013). Other basic reduction techniques use a minimum feature depth and/or area to filter artificial depressions introduced in the LiDAR processing and interpolation.

A raster sink-fill layer comprises continuous data that show gradual drainage and do not properly delineate the shape or perimeter of surface features. Appropriate data reduction of the raster fill layer allows for conversion to an accurate polygon layer that contains inherent geographic properties and delineated boundaries. A karst feature polygon layer enables the derivation of morphometric parameters of depressions such as circularity index, elongation ratio, and sinkhole long axis azimuth that can be used as quantifiable characteristics to identify patterns and provide insight on the genesis of karst landscapes (Day, 1983; Bondesan et al., 1992; Gutiérrez-Santolalla et al., 2005; Al-kouri et al., 2010; Basso et al., 2013; Kobal et al., 2015, Šegina et al., 2018).

Many factors have been described for karst development, with certain elements contributing to higher rates of limestone dissolution (Theilen-Willage et al., 2014). Causal factors, such as slope gradient, curvature, lithology, and groundwater table levels determine favorability conditions and can be analyzed with DEM overlays in ArcGIS (Theilen-Willage et al., 2014). Triggering factors, such as the rate of precipitation and water acidity, determine timing of speleogenesis and karstification (Theilen-Willage et al., 2014). Depressions, the most common surface karst feature in the region, have been mapped using a variety of methods. The most accurate method of surface karst mapping to date is to use an automated function to find all closed basins with no surface outflow, followed by careful corrections from an expert geomorphologist to show only the features attributable to karst processes (Day, 1983; Bondesan et al., 1992; Gutiérrez-Santolalla et al., 2005; Al-kouri et al., 2010; Basso et al., 2013; Kobal et al., 2015, Šegina et al., 2018, Zumpano et al., 2019). Semi-automated mapping in this manner provides consistent, reliable results in terms of feature count, dimensions, and morphometric characteristics of surface karst features. (Doctor and Young, 2013; Zumpano et al., 2019). The shape of karst depressions is also dependent upon the dominant processes that lead to the formation of each particular feature, with coastal processes accelerating the development of sinkholes and the dissolution of carbonate rocks (Basso et al., 2013; Baichtal, 2021).

2.3 Geologic Setting of Southeast Alaska

Southeast Alaska's basement geology comprises terranes, regionally fault-bounded blocks of continental fragments and oceanic islands, that have been accreted onto a continent via tectonic drift. Prince of Wales Island is part of the Alexander Terrane, one of five subcontinental accreted geologic terranes in Southeast Alaska

containing numerous faulted blocks of limestone with intense karstification (Gehrels and Berg, 1992; Gehrels and Berg, 1994; Baichtal and Swanston, 1996; Colpron et al., 2007; Hendrickson and Groves, 2011; Pecha et al., 2016). These terranes are remnants of land masses with distinctive geology that were "smeared" onto present day southeast Alaska by oblique collision caused from partial strike-slip faulting and partial subduction of the Pacific Plate beneath the North American Plate during the mid-Cretaceous Period (Connor, 2014). This accretionary process forms northwest-southeast trending linear terranes that comprise the islands and mainland coast of southeast Alaska.

The majority of karst-forming lithology in the study area comprises the Heceta Limestone, a Silurian-aged rock unit, deposited in island intertidal to shallow subtidal conditions approximately $5° - 10°$ north or south of the equator in the paleo-Pacific Ocean (Soja, 1993). These sediment deposits represent carbonate sediments accumulated on a shallow water platform in an island arc setting (Soja, 1991; Soja, 1993). Large, extensive stomatolitic buildups represent quiet, restricted depositional areas that later slumped and brecciated with platform collapse relating to eustatic change and active tectonism during deposition (Soja, 1993). The Heceta Limestone Formation originated in an island-arc setting that accumulated contemporaneously with the Klakas Orogeny of the Ludlow epoch in the Silurian Period (Soja, 1993). This island later accreted onto the North American Craton during the mid-Cretaceous Period (Connor, 1988; Soja, 1993; Gehrels and Berg, 1992; Gehrels and Berg, 1994; Colpron, 2007; Pecha et al., 2016). Evidence of carbonate platform development is preserved in the variety of shallow-to-deep water limestones and interbedded polymictic conglomerates that make up the Heceta Limestone exposed on Prince of Wales Island (Soja, 1993). This evidence of

platform carbonates and extraordinarily thick (up to 1200 m) limestone deposits in Alaska results from a proximity to the paleoequator, as well as conditions favorable for widespread carbonate precipitation during the Silurian Period (Soja, 2008). Tectonics during island accretion caused thrust faulting and replication of section of the Heceta Limestone, leading the formation to originally be identified as over 3000 m in thickness (Baichtal, 2021). Due to the complex tectonic events that occurred during sediment accumulation and subsequent accretion of the island-arc carbonates, much of the Heceta Limestone shows periodic disruptions of carbonate deposition and brecciation events of the stromatolitic buildups that form large portions of the formation (Soja, 1990). Much of the massive limestone has been recrystallized, resulting in extremely pure, sparite-rich carbonate rock. While the strike and dip of limestone deposits in southeast Alaska vary from section to section, they typically have a shallow dip of approximately $18 - 40$ degrees (Soja, 1990).

2.4 Karst Formation on Prince of Wales Island

The features and three-dimensional nature of karst landscapes result from the interaction between geology, climate, topography, hydrology, and biological factors over geologic time scales. Alaska's karst landscapes are of particular interest due to intense geologic variation, well-developed karst systems, and the hosting of coastal temperate rainforests; a combination of factors seen only in select regions on Earth such as coastal British Columbia, New Zealand (South Island), and Tasmania (Aley et al., 1993; Griffiths et al., 2002; Ford and Williams, 2007). The oblique collision of the terranes onto the North American craton by northwest-southeast trending partial transform faulting created fractured bedrock that has been shown to control the formation of karst features (Baichtal

11

and Swanston, 1996). This highly fractured, pure carbonate bedrock, coupled with a mid-latitude, oceanic climate with high rainfall, leads to extremely rapid karstification (Figure 4) (Ford and Williams, 2007; White, 2007). The Heceta Limestone is typically massive-to-thickly bedded, with conduits more often forming along structural breaks as opposed to folded beds. Multiple continental and alpine glaciations during the Pleistocene epoch (2 mya – 10 kya) have led to large scale erosional and depositional events, resulting in an extremely modified landscape (Harris et al., 1974).

There is evidence that many caves existed prior to the Last Glacial Maximum (LGM; ~26 – 19 kya in the area), including the presence of glacial sediments, wood, and Pleistocene vertebrate remains found inside the caves (Baichtal and Swanston; 1996, Lesnek et al., 2020). However, evidence such as sinkholes formed around glacial sediment deposits, indicates either rapid post-glacial karstification or the continuation of karstification that occurred prior to the LGM. Evidence for the exact timing for terrestrial retreat of the Cordilleran Ice Sheet (CIS) that covered southeast Alaska during the LGM is still somewhat scant. Recent [10]Be ages from bedrock and glacial erratics, coupled with ^{14}C ages from raised marine sediments suggest that the easternmost portions of southeast Alaska were ice-free by the start of the Holocene, ~11.7 kya (Lesnek et al., 2020).

Figure 4. Examples of Typical Surface Karst Features on Prince of Wales Island; perspective from the base of a large sinkhole on north Prince of Wales Island (Left) and a karst window in a cave (Right).

Alaskan muskegs are areas with poorly drained soils containing acidic (2.1 – 5.5 pH) waters held in place by slowly decaying sphagnum moss (Harris et al., 1974). The low pH waters draining from Alaskan muskegs have led to the fastest recorded carbonate stream downcutting rate in the world at 1670 mm/ka (Allred, 2004; White, 2007). Muskegs are prevalent in karst areas in southeast Alaska due to deposition and compaction of impermeable glacial till in depressions that predate the LGM (Baichtal and Swanston, 1996; Lesnek et al., 2020). The existence of till-underlain muskegs in areas of carbonate bedrock allows for allogenic drainage of organic acid-rich water directly into

karst systems, resulting in accelerated karstification (Harris et al., 1974; Allred, 2004; White, 2007). Muskegs most often form relatively flat areas, however, muskegs in southeast Alaska have been found to form slopes as steep as 22°, which can provide downslope karst systems with consistently large quantities of corrosive runoff (Harris et al., 1974). Alaskan karst is also known for sinkholes that coalesce into larger features known as uvalas. Uvala is a term that denotes a closed karst depression with compounded sinkholes that typically covers a larger surface area, has a more elongate morphology, and contains greater depression depth than individual sinkholes.

3.0 STUDY AREA

The study area used for analysis comprises all the mapped karst on Prince of

Wales Island above 55.65 degrees latitude (Figure 5). The 55.65-degree latitude line is a

somewhat arbitrary location that roughly defines the northern half of Prince of Wales

Island, encompassing all of the areas that were manually surveyed for this study. Prince

of Wales Island comprises one of the more remarkable karst regions in Alaska due to the

sheer number of karst features present (Figure 1). The mapped karst in the study region

covers a total area of ~420 km^2. The region has been heavily influenced by past tectonics

and continental glaciations (Baichtal and Swanston, 1996). Southeast Alaska's climate is

defined as coastal maritime; characterized by cool, moist summers and moderate winters

(Köppen, 1984). The low annual temperature ranges and high average precipitation

categorize southeast Alaska as a temperate rainforest, dominated primarily by western

hemlock and Sitka spruce with lesser amounts of western redcedar and Alaskan yellow

cedar that become more scarce further north in the region (Harris et al., 1974). Low

average temperatures and high rainfall inhibit plant decomposition, resulting in an

abundance of acidic peatlands, known as muskegs, interspersed throughout forest stands

(Harris et al., 1974). Southeast Alaska is also known for the abundance of plant life, with

scarcely any of the land besides vertical cliff faces devoid of vegetation (Harris et al.,

1974). The landscape is characterized by coarse drainage patterns with deep valleys,

steep slopes, and narrow intervalley ridges, all strongly controlled by bedrock faulting

and heavily modified by extensive glaciations (Harris et al., 1974). Continental

glaciations have restructured the surficial geology of nearly the entire study area,

grinding away and collapsing preexisting karst systems and depositing large amounts of

glacial sediments atop and inside of karst features (Baichtal and Swanston 1996). The complex geologic and geomorphic history of the region complicates karst feature prediction and analysis by covering or exhuming karst features depending on the amount of sediment transported and deposited by the ice sheets, the lithology of the island crust being overran, the preexisting topography, and numerous other factors that play into the evolution of karst in such a geomorphically dynamic area.
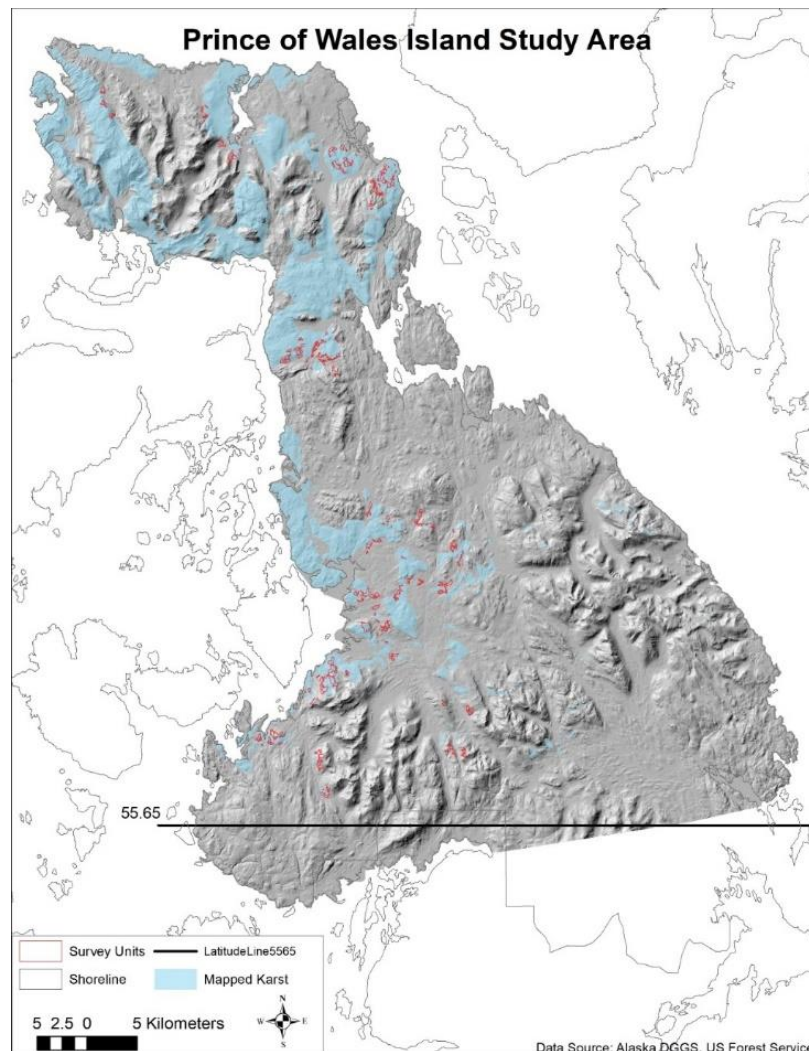
Figure 5. Reference Map of the Extent of Bare-Earth LiDAR Imagery in Hillshade for the Study Area Portion of Prince of Wales Island. Light blue polygons highlight the mapped carbonate bedrock and red polygons delineate the areas ground-surveyed for comparison during this project. (Centroid: -133.093430, 56.006933 Decimal Degrees)

4.0 METHODS

4.1 LiDAR Imagery

A cooperative effort between the US Geological Survey and US Forest Service in

Alaska collected the high-resolution LiDAR imagery used by this study in the summer of

2017. This bare-earth DEM dataset is publicly available and can be obtained from the

Alaska Division of Geological and Geophysical Surveys website in 2 km by 2 km

imagery tiles (DGGS, 2013). The Tongass National Forest and Sitka Conservation

Society provided the dataset as a seamless DTM to enable faster and more complete

analysis. This mosaicked, uncompressed file retains extremely detailed imagery allowing

for identification of the often small, yet hydrologically significant, karst depressions

found in the area while allowing for analysis on a large scale (Figure 6). The 32-Bit

floating-point dataset comprises 0.5 m-pixel resolution, with 194,515 columns and

296,500 rows in an uncompressed file size of 214.85 GB, although only the Prince of

Wales Island extent of the dataset is used (Figure 4). The vertical datum for this imagery

is the mean high tide line for southeast Alaska, with elevations ranging from -0.55 m to

1022.4 m.
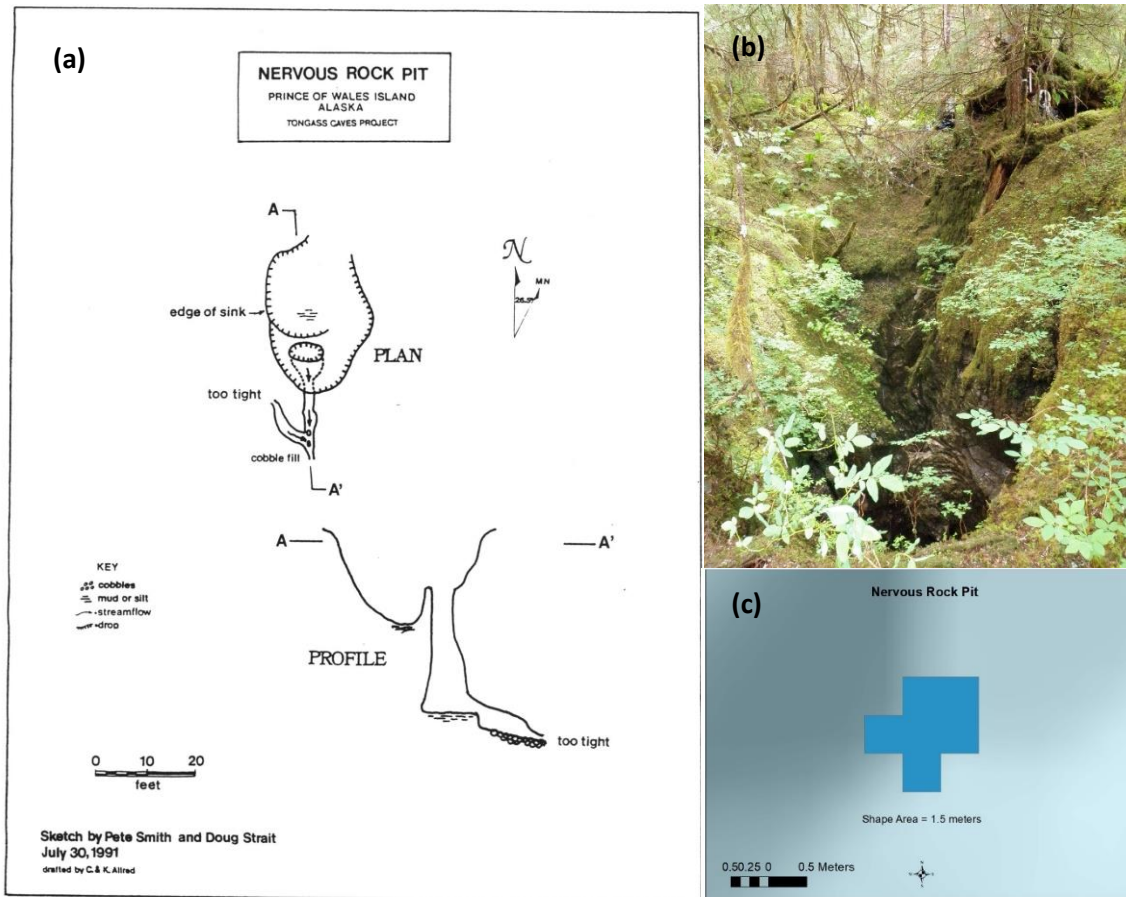
Figure 6. Example of a Legitimate but Atypical Karst Feature a) plan and profile map of Nervous Rock Pit, a small but hydrologically significant karst feature; b) entrance to Nervous Rock Pit (credit: Jim Baichtal); c) map showing depression polygon of Nervous Rock Pit with a area of 1.5 m^2.

4.2 Projections

The DTM imagery is in the Geographic Coordinate System NAD 1983, projected in the State Plane Alaska 1 FIPS 5001 (US meters) coordinate system (2011). The projection specifically used is the Hotine Oblique Mercator (HOM), also known as oblique cylindrical orthomorphic. The HOM projection is an oblique rotation of the Mercator projection with an azimuth of -36.87 degrees, a center longitude of -133.67 degrees, and a center of latitude of 57.00 degrees (ESRI, 2019). This projection retains

shape, direction, and local angular relationships, with area and distance increasing in distortion with distance from the central standard parallel. The HOM projection is often used to map obliquely oriented areas that do not follow a north-south or east-west trend, such as southeast Alaska (Figure 7) (ESRI, 2019). The HOM Projection is used for all maps and datasets in this study.
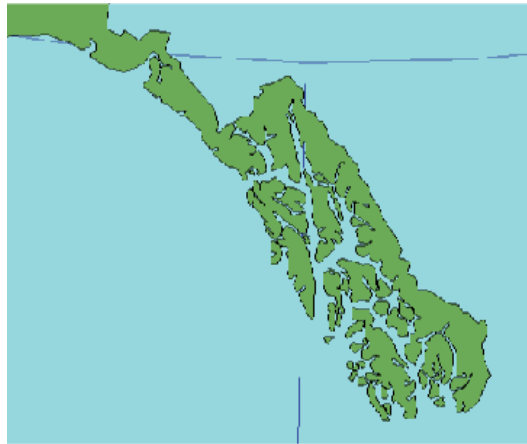
Figure 7. Map of the Hotine Oblique Mercator projection created specifically for the Panhandle of Alaska due to the oblique angle of the region (ESRI, 2019).

4.3 Karst Feature Delineation and Prediction

Delineation of karst features in a high relief, densely vegetated terrain has changed over the last 35 years from stereoscopic analysis of air photographs, through the evolution of handheld GPS, to GIS imagery and reconditioning tools. The acquisition of high-resolution LiDAR and its reconditioning to define karst features is in the process of changing field reconnaissance from search and discovery efforts to field verification, a more focused and significantly less time-consuming process. Field data represents collection by karst technicians conducting surveys on proposed Forest Service timber harvest units over three field seasons between 2017-2019. A Garmin® Oregon 650t with $\sim 5 - 10$ m accuracy error was used to record tracks and waypoints of karst surveys. These

GPS data had 100 ft buffers placed around each karst feature point within ArcMap, corresponding with a flagged buffer on the ground, representing high vulnerability (HV) karst areas. Inconsistencies exist in the accuracy of data between the vector mapped polygons and the implementation on the ground, such as the buffers being applied to points as opposed to polygon basins (Figure 10d).

4.4 Overview of the Semi-Automated Approach

This method for delineating karst depressions is a semi-automated approach comprising several steps: (1) DTM filtering; (2) identifying karst depressions using the priority-flood algorithm; (3) removing noise using minimum depth thresholds; (4) converting raster data into polygon feature data; and (5) filtering noise and non-karst depressions using automated and manual processes. Additionally, geometric attributes for each karst depression have been calculated to conduct preliminary analysis on a large morphometric dataset.

4.4.1 DEM Filtering

All digital elevation data contain some level of uncertainty and error that arises during various steps in the DEM creation process, such as data collection, processing, and interpolation (Fisher and Tate, 2006). DEM errors can occur in both the elevation or vertical (Z) and planimetric or horizontal (XY) coordinates, but focus is typically on vertical error, since planimetric error will produce elevation error, but not vice versa. Errors in DEMs can generally be grouped into three categories: 1) gross errors, 2) systematic errors, and 3) random errors (Liu and Jezek, 1999; Oksanen, 2003, Fisher and Tate, 2006). Gross errors result from poor experimental technique or mistakes in the measurement process (Oksanen, 2003; Fisher and Tate, 2006). Systematic errors arise

during the data collection process and tend to be consistent in magnitude and direction. Gross and systematic errors are typically corrected before the DEM is released (Li et al., 2011). Random errors vary in magnitude and direction, making them difficult to detect, especially on large, high-resolution datasets. As a result, random errors are usually left uncorrected and are inherent in the DEM. Due to these errors, it is common practice to suppress "data noise" by smoothing the DEM before using it to conduct terrain analysis and hydrological modeling (Wu et al., 2019). There are numerous ways to smooth DEMs with filters; this study utilized the ArcGIS Focal Statistics Tool to apply a three by three-pixel, rectangle median filter to preserve as much high-resolution data as possible, while reducing random error (after Wu et al., 2019). The high relief topography, coupled with the high density of karst features in southeast Alaska, requires minimizing the smoothing to retain as many of the small, yet hydrologically significant surface karst features as possible (Figure 6).

4.4.2 Identifying Depressions Using Priority-Flood Algorithm

The high resolution and large size of the bare-earth DEM requires the primary steps of the model to be conducted on fragments of the dataset. After generating the smoothed DTMs for all parcels of land on Prince of Wales Island with mapped karst above the 55.65 degrees latitude line, the Hydrology Fill Tool (i.e., priority-flood algorithm) from the ArcGIS Spatial Analyst Toolset identifies and fills all hydrologic sinks, resulting in a depressionless DEM (Wang and Liu, 2006; Doctor and Young, 2013, Wu et al., 2019). Then, the original, smoothed DEM is subtracted from the filled DEM to create a dataset composed entirely of depressions, with each grid cell representing depression depth in meters from the spill-line (Doctor and Young, 2013; Wu et al., 2019).

21

Grid cells with zero (0) difference value are automatically eliminated from further analysis during this step.

4.4.3 Removing Noise Using Minimum Depth Thresholds

Since depressions in a DEM are commonly a combination of artefact, artificial, and natural depressions, certain factors can remove small and shallow sinks from the sink-fill difference layer to result in a more meaningful dataset (Lindsey and Creed, 2006; Wu et al., 2019). The Set Null Tool from the ArcMap Spatial Analyst Toolset is used to set minimum depth thresholds (MDTs) of 0.3 m and 0.5 m for overlap comparison. This removes every depression with a depth shallower than the input value while retaining all depressions that fit the depth criteria. The Set Null Tool works to remove a large amount of noise caused by shallow irregularities in the high-resolution data, as well as minimizes the dataset size and allows for faster computation of the karst feature prediction model.

4.4.4 Converting Raster Data into Polygon Feature Data

Bare-earth DEMs created from LiDAR point clouds comprise continuous, high resolution data, with each 0.5 m by 0.5 m grid cell containing up to 20 decimal places. Continuous elevation data cannot be directly converted to discrete polygons or contours. For the early steps of the semi-automated approach, only the feature boundaries are necessary to extract from the sink-fill raster layer. These polygon subsets are later appended into one large polygon dataset to be used as a mask to clip the original DEM. The depression depth values must be grouped into integer categories before the conversion from raster to polygon can take place. The Reclassify Tool from the ArcGIS Spatial Analyst Toolset groups raster values into two meter-interval subgroups. A two-meter defined interval reclassification method allows for retention of depth for each

feature. Once reclassified, the Raster to Polygon Conversion Tool creates unsimplified polygons that directly overlap with the original raster dataset. These feature polygons delineate the immediate catchment basins and contain inherent geographic and morphometric attributes that did not exist in the original raster dataset.

4.4.5 Filtering Noise and Non-Karst Depressions Using Automated and Manual Processes

After conversion, individual attributes and proximal locations further filter noise from the karst feature model. Comparisons of models use several combinations of depth and area filters for accuracy determinations. Minimum Area Thresholds (MATs) of 0 m^2, 1.0 m^2, 2.0 m^2, and 3.0 m^2 are applied across multiple datasets using 'select by attributes' on the Area field within ArcMap (Table 1). Zones where the data shows consistent, predictable error are located where surface streams meet roads. Unless every road and culvert are "burned" or lowered in elevation to not appear as a hydrologic dam, ditches and areas where surface streams run through culverts beneath roads will appear as closed depressions with no drainage (Figure 8b). While it is possible that some roads were built near or overtop of legitimate karst features, the majority of these are erroneous features and must be manually removed from the dataset (Figure 8). Gravel quarries are also often erroneously identified as depressions and must be manually removed (Figure 8a). A 'select by location' query identifies all polygon features within two meters of the Forest Service *Roads* GIS layer. Not every feature that is selected by this query is deleted; the tool is used to detect likely erroneous features, which are then manually examined and deselected if they have potential to be karst features.
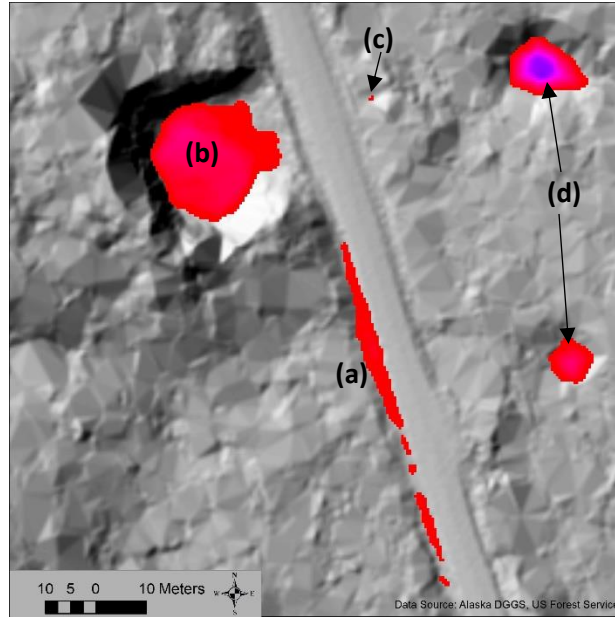
Figure 8. Examples of various false and true positive karst features in raster format with an MDT of 0.3 m displayed overtop a LiDAR hillshade; a) false positive features interpreted from ditches along a road; b) a false positive feature interpreted from a road quarry; c) a minute feature likely stemming from interpolation error that is filtered out through an MAT; d) features that fit all criteria for surface karst in this methodology and do not get removed from the layer. (Centroid: -133.253280, 56.103747 Decimal Degrees)

4.5 Predictive Model/Field Survey Agreement

To measure agreement between the karst feature prediction model and karst field surveys, karst polygons are buffered with a 100-foot HV buffer and analyzed using the Union Tool for overlap with the HV buffers derived from field reconnaissance. The Union Tool provides an FID number that describes polygon overlap between the datasets being analyzed, which is used to create a field that splits the dataset between three criteria: 1) automated buffer only, 2) field-mapped buffer only, and 3) automated and field-mapped buffer overlap. Comparisons are made between five karst vulnerability prediction models and previously field-mapped HV karst. Model A uses a depression MDT of 0.5 m, and Models B, C, D, and E use an MDT of 0.3 m. The five models are

compared for overlap with karst field surveys using no MAT, and varying MATs (1.0 m^2, 2.0 m^2, and 3.0 m^2).

These models are compared to the mapped HV karst clipped by a dataset of areas field-surveyed within the past 4 years to determine karst vulnerability with regard to timber sales. These units provide a delineated area that has been recently mapped and ground surveyed for karst features to determine overlap with the vulnerability models. Field-mapped HV karst features include: 1) where surface water directly infiltrates the subsurface karst systems, 2) areas directly over known cave passages, 3) areas where epikarst relief is greater than 8 ft, and 4) spring resurgences where water exits the subsurface. Some areas that were determined HV by ground-surveying, such as spring resurgences and 100 ft minimum buffers drawn 0.25-mile upstream from surface stream insurgent points required by the Forest Service guidelines, do not appear as HV through the automated method of this study. This technique is limited by identifying only closed depressions in karst-forming rock, where water can enter the subsurface. Because depressions are the most common form of surface karst in the region, this analysis should identify a significant portion of the vulnerable karst features. The karst vulnerability layer used by the Forest Service has been mapped by evolving methods over the course of 20+ years; so, while there are extensive karst areas mapped for HV, only the recently ground surveyed, GPS-mapped areas are used for direct comparison due to data integrity concerns.

4.6 Normalizing Polygons by Depth

Uvalas complicate GIS analysis by encompassing multiple hydrologic insurgences into relatively large, singular depressions that must be reconditioned to show

the deepest portions of each feature, where water is most likely to enter the subsurface. The depth grid codes derived from the original sink-fill raster remain after transitioning to the polygon features but do not exhibit the deepest portion relative to each feature. The method developed for normalizing sink-fill polygons utilizes the Spatial Analyst Zonal Statistics Tool to find the max sink-fill depth for each karst feature. The original sink-fill raster is then divided by the zonal statistics max depth using the Raster Calculator Tool to normalize the values for each feature, creating a raster with values ranging from $0 - 1.0$. The normalized raster is then reclassified to values $1 - 10$, with 10 being the deepest 10% of each feature. Once reclassified, the raster is then converted back to a polygon layer using the Raster to Polygon Tool, allowing for selection by attributes. For a layer with such large extent and number of features, any different selection of the deepest percentage will alter the size and number of insurgences found throughout the layer. For example, an uvala with an especially deep insurgence may still not show a secondary insurgence if the two vary greatly in relative depth, even if a second insurgence is present. This method accurately delineates the portion of each depression that is most likely to contain openings to subsurface hydrologic conduits. The deepest 20% of each feature was selected as the insurgent area, which is then converted to points using the Data Management Feature to Point Tool. Thia point file is then used to create a karst feature density map using the Spatial Analyst Point Density Tool with an output cell size of ten, circular neighborhood, 200 m radius, and square kilometer area units.

4.7 Morphometric Analysis

An analysis of depression morphometric attributes offers insight into the geomorphology of karst systems and how the associated hydrology and hazards will

26

continue to evolve (Williams, 1972). Morphometric properties are derived from the

dissolved boundary polygons layers created from Model D and Model E, as well as the

deepest 20% polygon layer created from the normalized Model D layer. These properties

include area, perimeter, circularity index (CI), length and azimuth of major and minor

sinkhole axes, and elongation ratio (ER) (Day, 1983; Basso et al., 2013). Spatial data for

these properties are automatically measured and stored in the dataset attribute table by the

Minimum Bounding Geometry (MBG) Tool and the Raster to Polygon Tool. The MBG

Tool is used with the "RECTANGLE_BY_WIDTH" geometry type and the "Add

geometry characteristics as attributes in the output" option to provide the spatial data

necessary to derive morphometric properties (Figure 9). The properties are then derived

from these data and analyzed in Microsoft Excel. Elongation ratio is calculated by taking

the ratio of sinkhole long axis over sinkhole short axis, providing an objective description

of sinkhole shape (Day, 1983; Basso et al., 2013). Circularity index is calculated where

A_m is the area and P_m is the perimeter of the depression as defined by the polygon feature

prediction model (Equation 1) (Kobal et al., 2015).

$$Circ_i = \frac{A_m}{\pi \cdot \left(2 \cdot \frac{A_m}{P_m}\right)^2}$$

(Equation 1)

CI provides a quantitative method of calculating "circularity" of individual

depressions and is defined by the deviation of a polygon from a perfect circle, which will

have a CI = 1.0. (Kobal et al., 2015). Large depressions and uvalas often have multiple

sources of water feeding into them, affecting the shape of depression boundaries

compared to features with only one source of surface water.
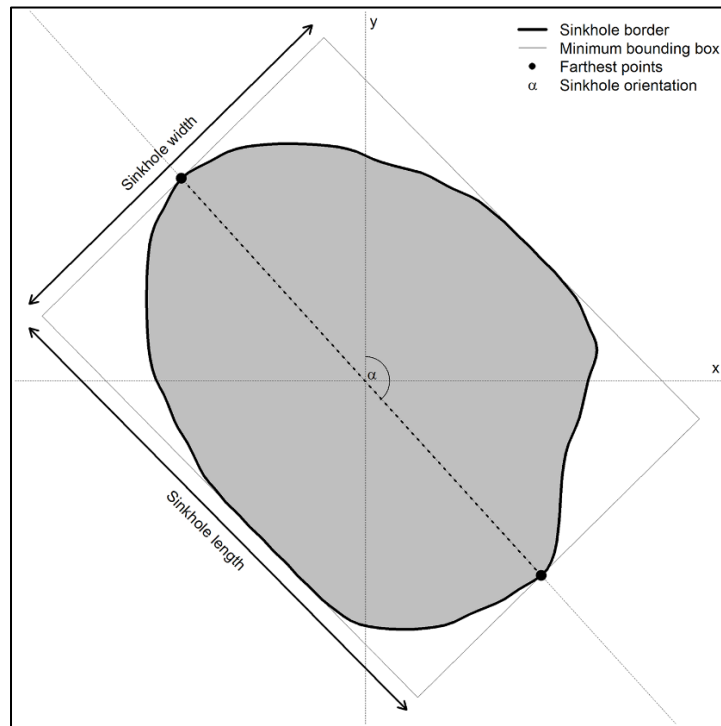
Figure 9. Illustration of measurements used to derive morphometric properties. Modified from Kobal et al., 2015. doi:10.1371/journal.pone.0122070.g003

5.0 RESULTS AND DISCUSSION

5.1 Comparison of HV Karst Derived from Prediction Models and Field Mapping

Due to the complexity of karst field surveys and high relief topography in the region, a one-to-one comparison of karst features is not appropriate for this study. Instead, agreement between the HV buffers derived from the various polygon models created during this study and previously field-mapped HV buffers is determined (Figure 10). GPS tracks from karst technicians assessing timber units for vulnerability allude to the time-consuming process of thorough karst surveys in southeast Alaska (Figure 10b). Inherent differences in manual versus automated methods of determining HV karst result in coverages that contain natural disparities. For example, karst springs often resurge from the subsurface on slopes and are not detected through automated means since spring resurgences typically do not form closed depressions. Sinking streams found in the field are also buffered 100 ft for HV 0.25-mile upstream from the point of insurgence, a distance that disregards topography and is impossible to fully automate in GIS without an extremely detailed hydrology layer. The consequence of these caveats is an inability to create a model that agrees 100% with the field-mapped only (FMO) HV karst (Figure 10). Manual karst mapping in the past also used points instead of polygons to inventory karst depressions due to the difficult and time-consuming nature of mapping depression boundaries in the field. The ability for automated karst feature mapping to capture and delineate depression boundaries results in a more realistic vulnerability map, with larger buffers drawn from the edge of depression polygons as opposed to a simple 100 ft buffer around a point for each feature (Figure 10d). These larger, polygon-derived HV karst

buffers account for a portion of the area that is covered by the automated models and not

the field-mapped method.
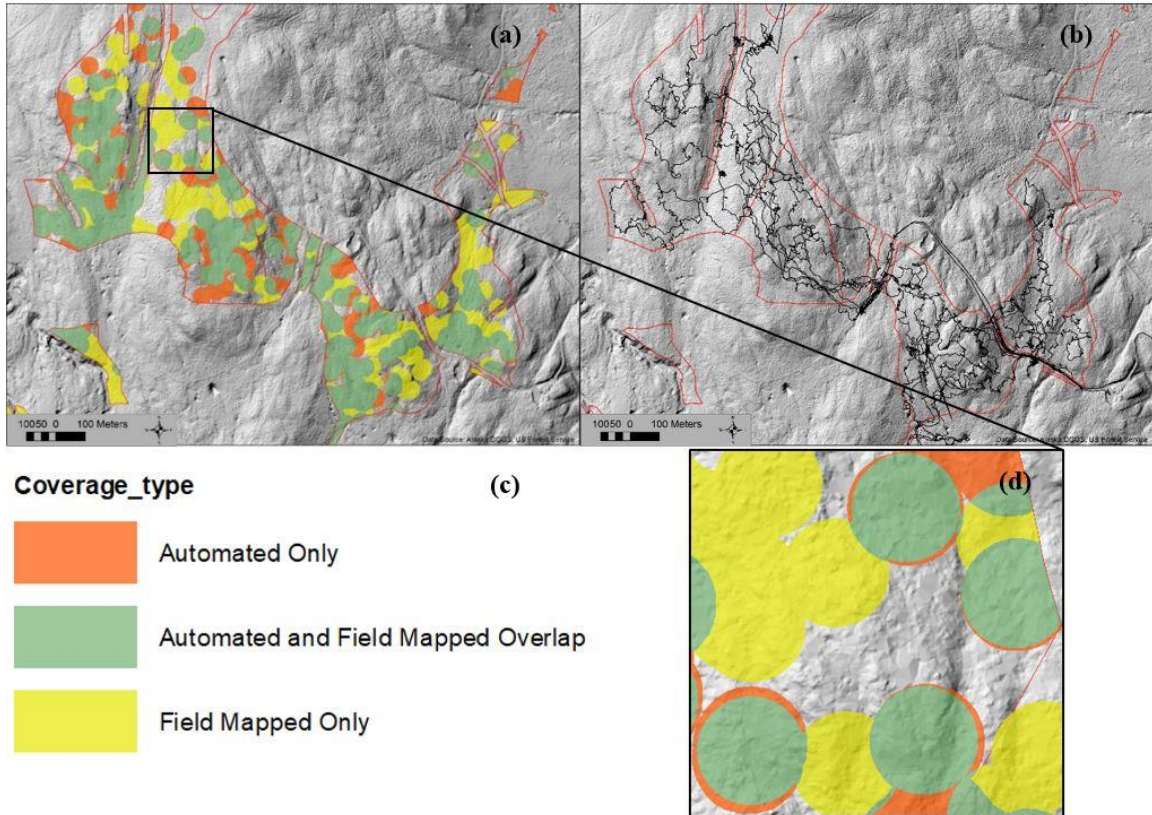
Figure 10. Subset of Delineated Area Used for Comparison of Overlap; a) Example of overlap between the field-mapped HV karst and the HV karst derived from Model D, using the 0.3 m MDT, 2.0 m^2 MAT clipped to potential timber unit boundaries; b) tracks from two karst technicians surveying potential timber units over three days for karst vulnerability; c) legend for types of overlap; d) overlap of coverage created from automated sink polygons versus field-mapped sink points. (Centroid: -133.093690, 56.230753 Decimal Degrees)

The five models in this study do not contain extreme variations in the size

thresholds used to filter the sink-fill layer (Figure 11). While the areas used for

comparison are considerably smaller in extent than the ~420 km^2 study area that was

mapped for karst features by the automated models, the small variations in threshold sizes

significantly alter the HV coverage from a land management perspective. The total area

of mapped karst clipped to field surveyed units and analyzed for agreement with the automated prediction models is 10.1 km^2 (Table 1). The amount of HV karst field-mapped for this clipped extent is about 2.3 km^2, or 22.4% of the area; a reasonable value considering the complexities of karst topography and hydrology in the region. An automated karst feature model that predicts locations and delineates highly vulnerable karst is a large step in the right direction with regards to properly understanding and managing the important resources associated with karst lands. As previously mentioned, none of these models are expected to display complete agreement and none are expected to fully cover the field-mapped only portion of HV karst. The automated portion of each model is also expected to identify features that were not detected manually due to areas that were missed during surveying, features delineated with polygon boundaries instead of single points, or depressions that fit the models but do not contain hydrologic insurgences. While existing karst feature inventory data are not extensive enough to conduct a one-to-one analysis on features determined through manual versus automated methods, a comparison of the number of depression polygons detected across the study area is used to assess the validity of each predictive model (Table 2).
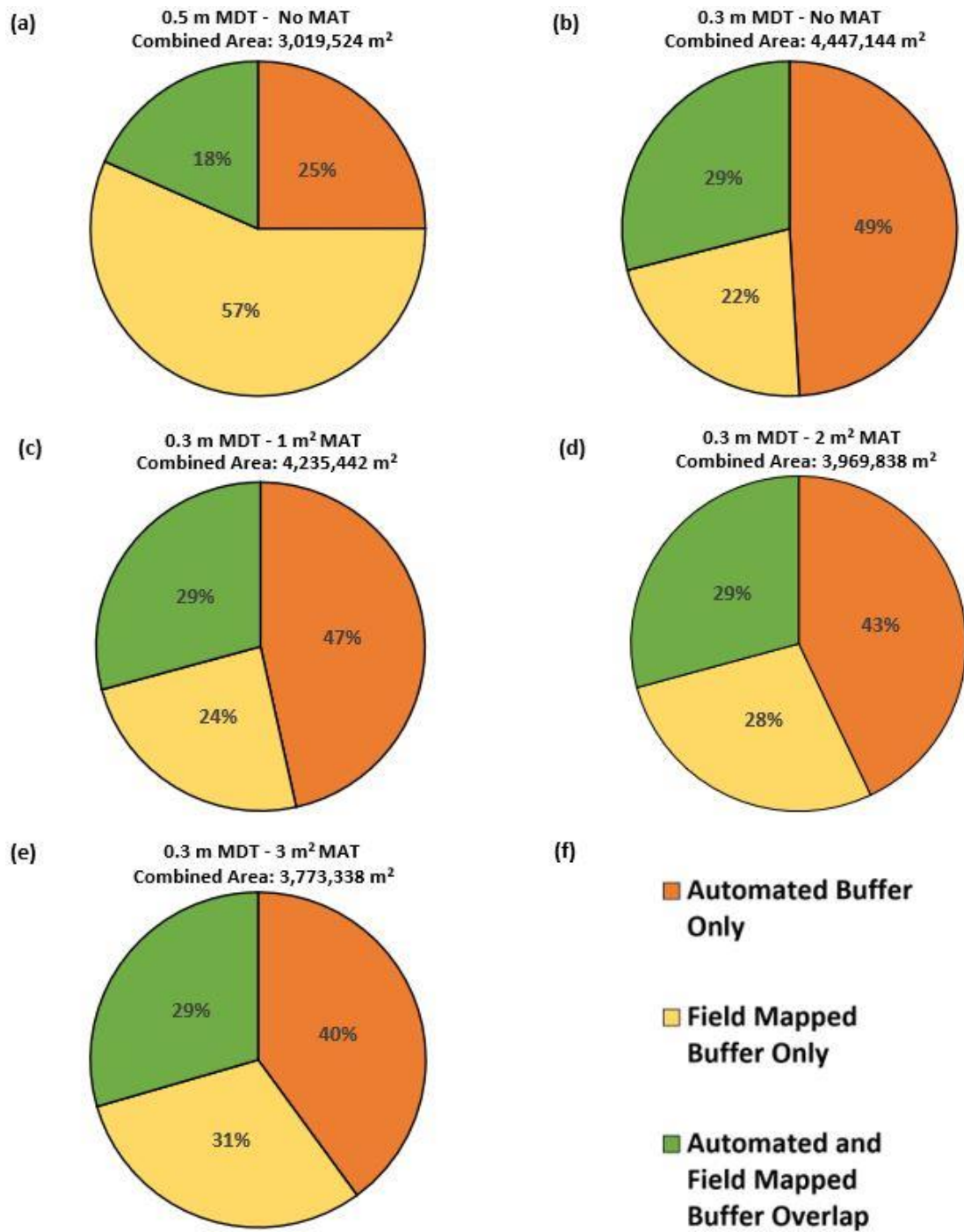
Figure 11. Overlap Percentage Between the Field-Mapped HV (FMHV) Karst and the HV Karst Mapped by the Five Automated Models; a) Model A with no MAT and an MDT of 0.5 m; b) Model B with no MAT and an MDT of 0.3 m; c) Model C with a 0.3 m MDT and 1.0 m^2 MAT; d) Model D with a 0.3 m MDT and 2.0 m^2 MAT; e) Model E with a 0.3 m MDT and 3.0 m^2 MAT; f) legend for overlap types.

Table 1. Mapped Karst Area Compared with the HV Karst Area Derived from the Various Models and Methods of Vulnerability Mapping.

	Area (m²)	HV Karst/ Mapped Karst Proportion (%)	Combined Automated and Field-mapped HV Karst/ Mapped Karst Proportion (%)
Mapped Karst (Clipped to Units)	10,107,288.5	—	—
Field-mapped HV Karst	2,262,383.8	22.4	—
Model A (MDT: 0.5 m)	1,309,967.5	13.0	30.9
Model B (MDT: 0.3 m)	3,470,795.1	34.4	44.0
Model C (MDT: 0.3 m MAT: 1 m²)	3,207,556.5	31.7	42.0
Model D (MDT: 0.3 m MAT: 2 m²)	2,864,203.6	28.3	39.3
Model E (MDT: 0.3 m MAT: 3 m²)	2,620,705.9	26.0	37.3

Table 2. Comparison of Number of Dissolved Depression Polygons Identified Across the ~420 km² Study Area for Each Predictive Model.

Predictive Models	Model A	Model B	Model C	Model D	Model E
Model A **(65,519)**	—	+54,785	+37,282	+21,448	+9,595
Model B **(120,304)**	-54,785	—	-17,503	-33,337	-45,190
Model C **(102,801)**	-37,282	+17,503	—	-17,834	-27,687
Model D **(86,967)**	-21,448	+33,337	+15,834	—	-11,853
Model E **(75,114)**	-9,595	+45,190	+27,687	+11,853	—

5.2 Model Descriptions and Comparisons

The layers and overlap types described in the following section are abbreviated for clarity: field-mapped high vulnerability (FMHV) describes the dataset of manually mapped high vulnerability karst; field-mapped only (FMO) describes areas that were deemed HV karst through field mapping and do not overlap with the automated coverage; automated only (AO) describes areas that were deemed HV through automated methods and do not overlap with the field-mapped coverage.

5.2.1 Model A

Model A has the following parameters: no MAT and an MDT of 0.5 m (Figure 11a). This model overlaps rather poorly with the FMHV layer and exhibits only 18% agreement, with an FMO of 57%, the highest FMO value observed throughout all the models. Model A encompasses only 58% as much HV karst area as that designated through field mapping, while the other models designate at least 14% more area as HV than is manually mapped (Table 1). This poor overlap suggests that the 0.5 m MDT is too large, misrepresenting the boundaries and depth of karst features in the region and underestimating the extent of HV karst without applying an MAT filter.

5.2.2 Model B

Model B has the following parameters: no MAT, MDT of 0.3 m (Figure 11b). This model overlaps by 29%, exhibiting better agreement relative to Model A. Out of all the models analyzed in this study, Model B encompasses the most area coverage, with 49% of the layer included in the AO portion and the FMO portion reduced from 57% in Model A down to 22% in Model B. The results and large extent of this model suggest

that much of the FMO portion is a small value due to incidental overlap, where Model B

covers so much area that it appears to correspond with a large portion of the FMHV. The

number of dissolved karst features identified between Models A and B also varies

considerably; with an increase of 54,785 karst features (84%) detected simply by

decreasing the MDT by 0.2 m (Table 2). The high-resolution nature of LiDAR elevation

data allows for the detection of small, yet hydrologically significant karst features that

have not been measurable with previous, lower resolution iterations of bare-earth imagery

(Figure 6). While it would be ideal to automate the inventorying of features down to this

size, for each true positive, minute feature identified, potentially thousands of erroneous

features are detected that stem from errors in imagery processing, interpolation, and slight

changes in elevation due to fallen trees and other forest debris interpreted as ground

points (Figure 8). Model B delineates markedly more HV karst area than Model A at

34.4% but clearly needs some amount of filtering to create a more meaningful predictive

model, as buffering every minute feature 100 feet generates a coverage with a noticeably

larger extent than that determined in the field.

5.2.3 Model C

Model C seeks to reduce the amount of noise in the prediction model and has the

following parameters: 0.3 m MDT value and an MAT of 1.0 m^2 (Figure 11c). This model

removes all features that are smaller than 2 by 2 0.5 m-pixels and begins to create a more

meaningful karst feature layer. The results of Model C do not differ considerably from

Model B, but the application of an MAT lowers the extent of coverage closer to that of

the FMHV layer and retains the 29% agreement, suggesting that a 1.0 m^2 MAT preserves

legitimate features and limits noise from the model. It should be noted that, while they

exist, a very limited number of karst features identified in the field are found in depressions smaller than 1.0 m^2.

5.2.4 Model D

Model D has the following parameters: 0.3 m MDT and an MAT of 2.0 m^2 (Figure 11d). Model D categorizes ~28% of the mapped karst as HV, a value closer to the FMHV karst percentage than is displayed by Models A, B, and C (Table 1). The 2.0 m^2 MAT used to filter this model removes 33,537 polygons from Model B, which shares the same 0.3 m MDT but uses no MAT (Table 2). There are known karst features that fall below this 2.0 m^2 area threshold, but less than one percent have been previously documented in the field (Figure 6). This suggests that, while missing some legitimate but atypical features, Model D limits noise created by buffering miniscule potential karst polygons for HV and provides a reliable predictive model for karst features.

5.2.5 Model E

Model E has the following parameters: 0.3 m MDT and an MAT of 3.0 m^2 (Figure 11e). This model continues to filter out some amount of false positive features, but the ratio of true to false features that are removed is higher with this size threshold than those used in the previous models (Figure 12). While the mapped extent of HV karst for Model E is closer to the FMHV extent relative to the other models, 3.0 m^2 is not an atypical size for sinkhole depressions in the region and numerous, verified karst features are filtered out when this MAT is implemented (Figure 12). However, it should be noted that all field-verified features filtered out between models D and E are in old growth forest, where LiDAR scanners are able to penetrate the canopy (Figure 12a). Dense

young growth forests obscure LiDAR scanners and contribute to zones of lower-resolution bare-earth data, where it is more likely for the polygons removed with a 3.0 m^2 MAT to be erroneous in origin (Figure 12b). Considering that most of the study area does not comprise the extremely dense young growth forest that greatly diminishes the efficacy of these predictive models, Model D uses the ideal size threshold combination to minimize noise and maximize karst feature prediction.
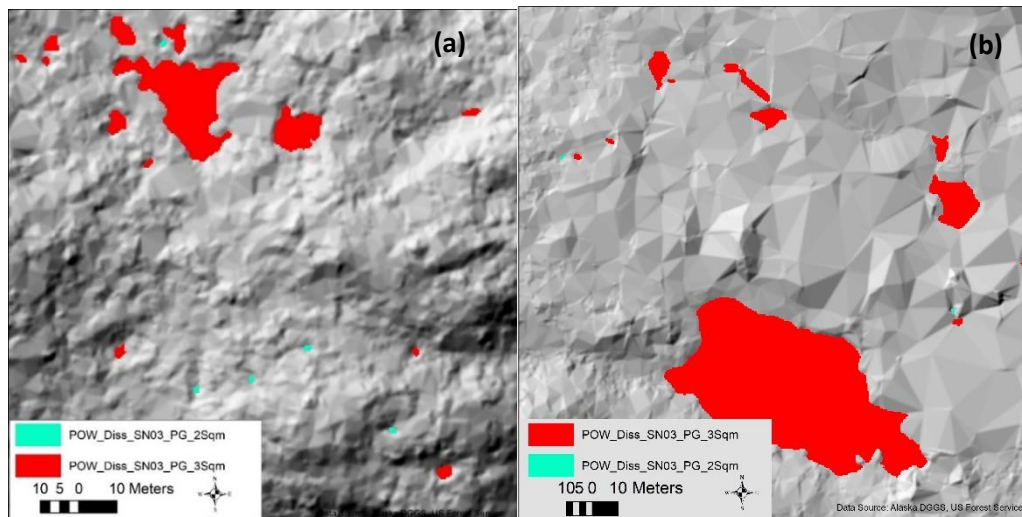
Figure 12. A comparison between the karst features detected by Models D and E, with an MAT of 2.0 m^2 and 3.0 m^2, respectively; a) beryl green polygons filtered by Model E that have previously been verified in an old growth forest area; b) beryl green polygons filtered by Model E in a dense young growth forest area that have not been field-verified. (Centroid(a): -132.867316, 55.712735 Decimal Degrees) (Centroid(b): -133.132969, 55.793812 Decimal Degrees)

5.3 Utilization of Model D

With Model D agreeing most with the FMHV layer while retaining the largest number of potential active karst features, the polygons resulting from a 0.3 m MDT and a 2.0 m^2 MAT are normalized and converted to points, using only the deepest 20% of each depression (Figure 13). Normalization by depth allows for the identification of the deepest portion of each karst depression, which can then be converted to points to

specifically locate areas where water is most likely to directly infiltrate the subsurface

(Figure 13). The normalization process is useful for analyzing compound karst

depressions, or uvalas, typical of developed surface karst in Alaska (Figure 13). While

the normalized polygons are useful for determining multiple insurgences in singular

depressions, the local topography within each depression strongly controls the accuracy

of determinations. Depressions with multiple insurgences that vary significantly in depth

will not properly capture every area of insurgence when only analyzing the deepest

twenty percent (Figure 13). Targeting the deepest 20% of the normalized polygon layer

balances the identification of multiple insurgences in uvalas with properly representing

the most likely area of insurgence (Figure 13). This process accurately captures the

deepest portion for each depression and is useful for converting polygons to point

features to determine points of insurgence and density of surface karst features across the

study area (Figures 13 and 14).
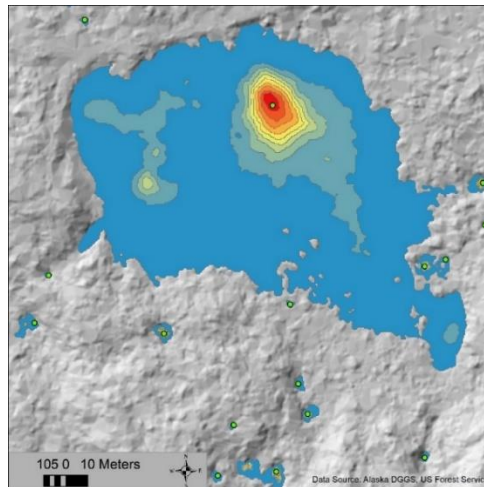
Figure 13. Example of Normalized Polygons. Normalized polygons capture depth relative to each karst depression, with points created at the center of the deepest 20% portion for each feature. The large depression is also an example of an exception to the proximal road filter, where the road in the northern portion of the figure intersects the boundary of a hydrologically active karst feature. (Centroid: -133.097264 56.224265 Decimal Degrees)
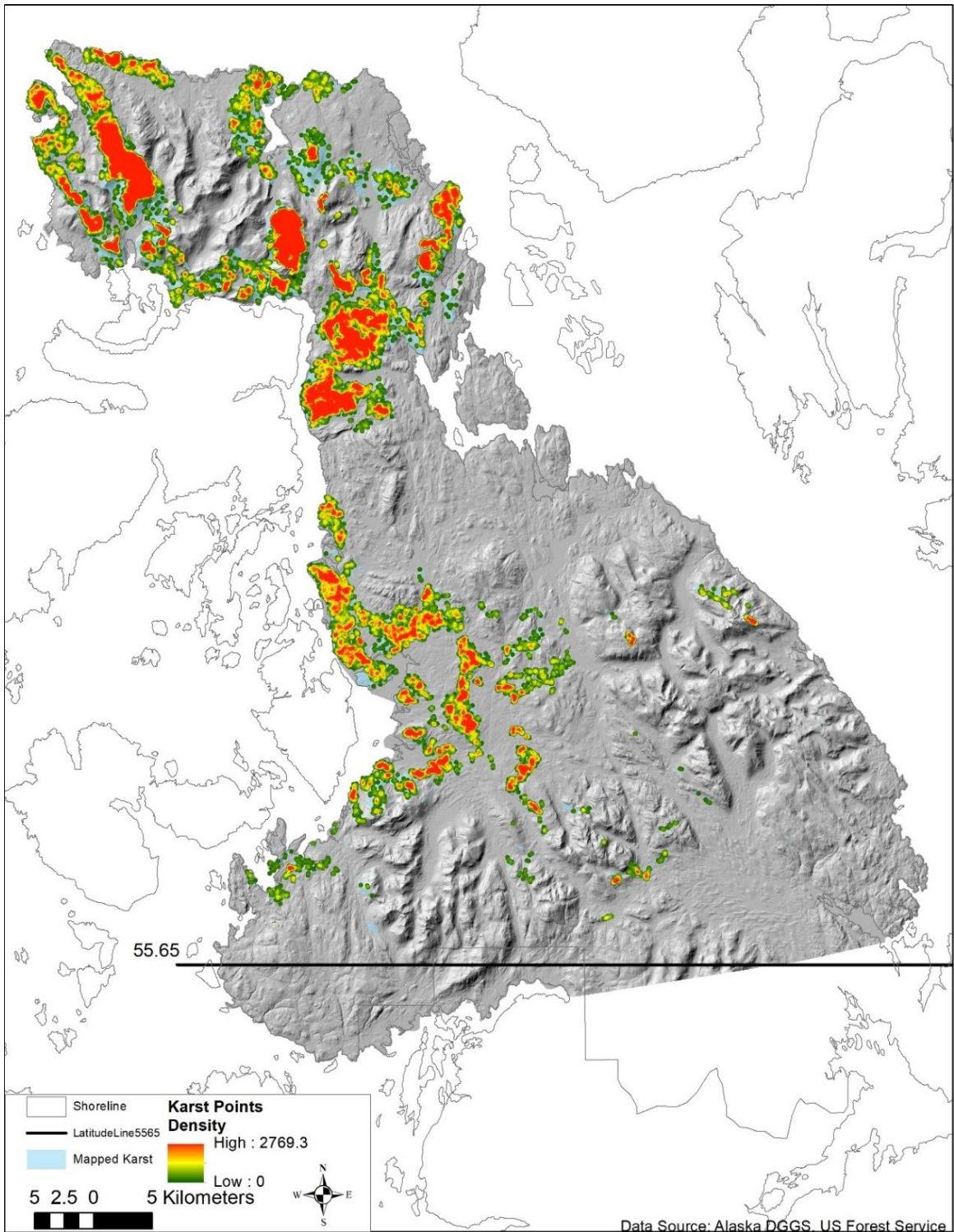
Figure 14. Karst feature density created using the Point Density Tool on the Normalized Feature-to-Point Layer from Model D, Displayed Over a LiDAR Hillshade.

The Point Density Tool creates a dataset of stretched values that display the density of karst features across the study area (Figure 14). The highest density of karst features identified through this process is 2,769.3 points per square kilometer. Upon visual inspection, the highest density areas are located at relatively high elevation areas with thick deposits of limestone (Figure 14). These high elevation, thick limestone deposits comprise vadose karst that forms from direct precipitation, where water largely travels in conduits directly downward, intersecting well beneath the surface of the landscape. The highest density of karst features is expected to occur in these areas, as they are typically not fed by streams and do not experience flooding, which results in less lateral widening than karst depressions at lower elevations. Vadose karst features are also deeper with steep sides, making them easier to detect through automated means. Low elevation karst depressions also more often form uvalas that are underestimated for number of insurgence points, even when normalized for depth.

5.4 Morphometric Properties of Features Identified by Semi-automation

Models D and E contain similar datasets, with the only difference comprising the polygons filtered between a 2.0 m^2 and 3.0 m^2 MAT, respectively (Figure 12). Minimum bounding boxes that capture feature axes lengths and long axis azimuths are used with feature attributes to derive morphometric properties for Models D and E, as well as the deepest 20% polygon layer for Model D (Figure 15). There is little variation between the morphometric averages derived from these models, with the largest difference found in the reduction of the average area by 26.8 m^2 from Model D to Model E. The average area for the deepest portions dataset from Model D is expectedly much lower than the dissolved boundaries for either model. The average ER and CI, however, are quite close

to that of the full boundary datasets, with some reduction in the average elongation of the

smaller polygons (10%) (Table 3). The average CI variations are small between the

datasets, but the results suggest that the deepest portions of the depressions are more

circular than the full depression boundaries. Interestingly, the average azimuth is quite

similar between the two models with different MATs but varies considerably with the

deepest portion dataset, suggesting an overbearing geologic control on karstification.
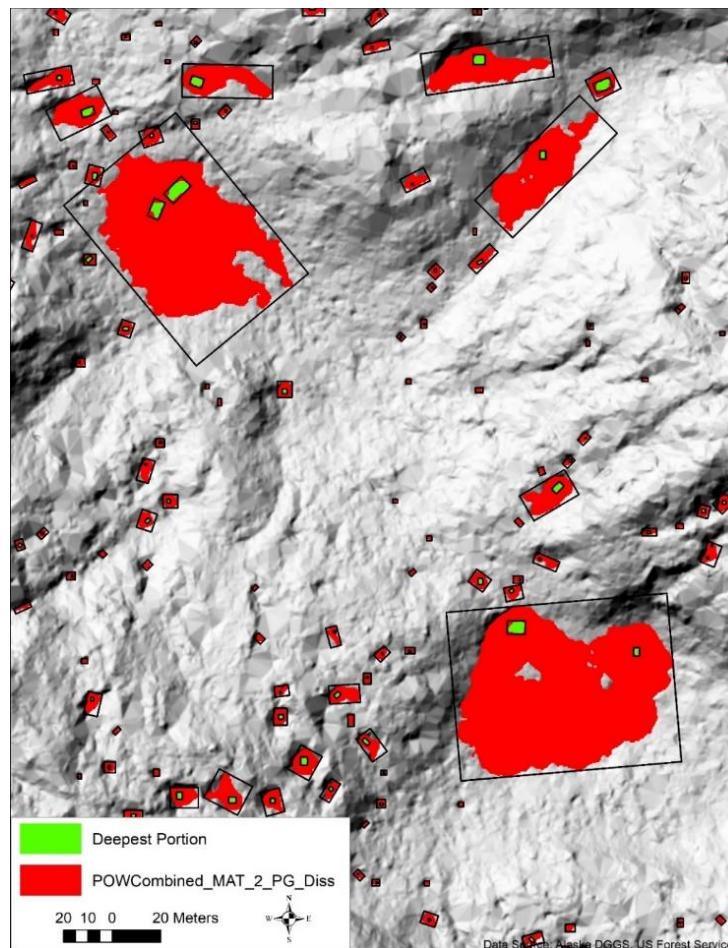
Figure 15. Dissolved polygons for the boundaries (Red) and deepest 20% (Green) of karst depressions from Model D, as well as the minimum bounding boxes derived with the MBG Tool (Black). (Centroid: -133.312429, 56.221999 Decimal Degrees)

Table 3. Some averages of morphometric properties derived from the dissolved polygons and deepest portion polygons from Model D and the dissolved polygons from Model E.

Polygon Dataset	Avg. Area (m²)	Avg. CI	Avg. Azimuth (°)	Avg. ER
Model D Boundaries n = 86,976	177.7	1.36	63	1.64
Model D Deepest Portions n = 53,556	5.84	1.34	37	1.47
Model E Boundaries n = 75,114	204.5	1.37	65	1.66

6.0 CONCLUSIONS

The high relief topography and complex hydrology of karst landscapes complicate karst feature surveying and inventorying in southeast Alaska. A reliable predictive model for identifying hydrologically active karst features determined from high-resolution LiDAR bare-earth imagery will advance karst management, recreation, conservation, and research in the region, while shifting karst surveys from a "search and discover" approach to a field-verification approach. This study analyzes a variety of filtration methods to determine the ideal size thresholds to minimize the detection of non-karst polygons while maximizing the detection of legitimate karst features. While there is some variation in predictive accuracy that relies on resolution consistency, the ideal model for karst feature detection in the region is Model D, which utilizes an MDT of 0.3 m and an MAT of 2.0 m^2. Model E, with an MDT of 0.3 and an MAT of 3.0 m^2, is also a reliable predictive model, but this model is shown to filter out legitimate karst features in areas of high-resolution imagery. For areas of reduced imagery resolution, such as dense young growth forest, Model E is a more ideal model to filter out as much noise as possible while maximizing the number of legitimate karst features.

Preliminary analysis of morphometric properties of karst depression polygons on Prince of Wales Island, Alaska suggest that further geostatistical investigation will provide insight into karst landscape evolution. This preliminary study did not seek to find patterns in the morphometrics of identified karst features. Instead, morphometric attributes were calculated to show one application of the dataset created with this semi-automated approach, with preliminary results suggesting that the underlying geology controls the development of surface karst features. Future geomorphology studies of this

43

karst area should focus on identifying correlations between various morphometric properties to determine the influence of factors such as fractures, faults, underlying geology, and surface processes on landscape evolution. These analyses may reveal factors that produce the interesting, complex karst features and topography found in the region. An accurate karst feature dataset of the size and resolution created during this study contains immense potential to progress interest and research in karst landscape evolution in a geomorphically active, yet understudied, portion of the world.

REFERENCES

Al-Kouri, O., Husaini, O., Abu-Shariah, M., Mahmud, A.R., Manso, S., 2010, Geostatistical Analysis of Karst Landscapes, Electronic Journal of Geotechnical Engineering.

Aley, T., C. Aley, W. Elliot, and P. Huntoon. 1993, Karst and cave resource significance assessment, Ketchikan Area, Tongass National Forest, Alaska, Final Report, prepared for the Ketchikan Area of the Tongass National Forest. 76 pp. + appendix.

Allred, 2004, Some Carbonate Erosion Rates of Southeast Alaska, *Journal of Cave and Karst Studies*, v. 66, no. 3, p. 89-97.

Antonellini, M., Nannoni, A., Vigna, B., & De Waele, J., 2019, Structural Control On Karst Water Circulation And Speleogenesis In A Lithological Contact zone: The Bossea Cave System (Western ALPS, ITALY). *Geomorphology, 345*, 106832. doi:10.1016/j.geomorph.2019.07.019

Audra, P., & Palmer, A. N., 2011, The pattern of caves: Controls of epigenic speleogenesis. *Géomorphologie : Relief, Processus, Environnement, 17*(4), 359-378. doi:10.4000/geomorphologie.9571

Baichtal, J.F., 1997, Application of a Karst Management Strategy: Two Case Studies from the Tongass National Forest, Southeastern Alaska The Challenges of Implementation. In 1997 Karst and Cave Management Symposium 13th National Cave Management Symposium. http://nckms.org/wp-content/uploads/2018/05/97nckmsall.pdf#page=10

Baichtal, J.F., 2021, Personal Communication.

Baichtal, J.F. and Karl, S.M., 2008, "Karst and Cave Development in Southeastern Alaska", for publication in "The Caves and Karst of the USA" Edited by Dr. Author and Margaret Palmer for the 15th International Congress of Speleology, July 19-26, 2009, Kerville, Texas.

Baichtal, J.F. and Langendoen, R., 2001, October. Lidar applications in a temperate rainforest environment-Case study: Kosciusko Island, southeastern Alaska, Tongass National. Forest. In Proceedings of the 2001 National Cave and Karst Management Symposium, Tucson, Arizona (p. 155).

Baichtal, J.F., Lesnek, A.J., Risa J. Carlson, R.J., Schmuck, N.S., Smith, J.L., Landwehr, D.J., and Briner, J.P., 2021, Late Pleistocene and Early Holocene Sea level History and Glacial Retreat Interpreted from Shell-bearing Marine Deposits of Southeastern Alaska, Geosphere (In Press).

Baichtal, J. F., & Swanston, D. N., 1996, Karst landscapes and associated resources: A resource assessment, US Department of Agriculture, Forest Service, Pacific Northwest Research Station. doi:10.2737/pnw-gtr-383

Barnes, R., Lehman, C., Mulla, D., 2013, Priority-flood: An optimal depression-filling and watershed-labeling algorithm for digital elevation models. Elsevier: *Computers and Geosciences.*

Basso, A., Bruno, E., Parise, M., and Pepe, M., 2013, Morphometric analysis of sinkholes in a karst coastal area of southern Apulia (Italy): Environmental Earth Sciences, v. 70, p. 2545–2559, doi: 10.1007/s12665-013-2297-z.

Bogli, A., 2012, Karst hydrology and physical speleology. In *Karst hydrology and physical speleology* (pp. 73-75). Springer-Verlag Berlin An.

Bondesan, A., Meneghel, M., and Sauro, U., 1992, Morphometric analysis of dolines: International Journal of Speleology, v. 21, p. 1–55, doi: 10.5038/1827-806x.21.1.1.

Bryant, M.D., Swanston, D.N., Wissmar, R.C. and Wright, B.E., 1998, Coho salmon populations in the karst landscape of north Prince of Wales Island, southeast Alaska. Transactions of the American Fisheries Society, 127(3), pp.425-433.

Chen, Z., Gao, B., and Devereux, B., 2017, State-of-the-Art: DTM Generation Using Airborne LIDAR Data: Sensors, v. 17, doi: https://dx.doi.org/10.3390%2Fs17010150.

Colpron, M., Nelson, J.L. and Murphy, D.C., 2007, Northern Cordilleran terranes and their interactions through time. GSA today, 17(4/5), p.4.

Connor, C., 2014, Roadside geology of Alaska: Missoula, MT, Mountain Press Publishing Company, p. 8-12.

Curry, William, "Using Cesium 137 to Understand Recent in Cave Sedimentation in the Tongass National Forest, Southeast Alaska", 2003, Masters Theses & Specialist Projects. Paper 589.

Day, M., 1983, Doline morphology and development in Barbados. *Annals of the Association of American Geographers, 73*(2), 206-219. doi:10.1111/j.1467-8306.1983.tb01408.x

DGGS Staff, 2013, Elevation Datasets of Alaska: Alaska Division of Geological & Geophysical Surveys Digital Data Series 4, https://maps.dggs.alaska.gov/elevationdata/. https://doi.org/10.14509/25239

Doctor, D., and Young, J., 2013, An Evaluation of Automated GIS Tools for Delineating Karst Sinkholes and Closed Depressions from 1-Meter LiDAR-Derived Digital Elevation Data: Full Proceedings of the Thirteenth Multidisciplinary Conference on Sinkholes and the Engineering and Environmental Impacts of Karst, doi: 10.5038/9780979542275.1156.

Environmental Systems Research Institute (ESRI), 2019, ArcGIS Desktop Help 10.7. https://desktop.arcgis.com/en/arcmap/10.7/map/projections/hotine-oblique-mercator.htm

Fisher, P.F., and Tate, N.J., 2006, Causes and consequences of error in digital elevation models: Progress in Physical Geography, v. 30, p. 467–489.

Ford, D. C., & Williams, P. W., 2007, *Karst hydrogeology and geomorphology*. Chichester: John Wiley & Sons.

Gehrels, G.E. and Berg, H.C., 1992, Geologic map of southeastern Alaska: US Geological Survey Miscellaneous Investigations Series Map I-1867.

Gehrels, G.E., and Berg, H.C., 1994, Geology of southeastern Alaska, in Plafker, George, and Berg, H.C., eds., The Geology of Alaska: Geological Society of America, p. 451-467.

Griffiths, P.; Aley, T.; Worthington, S.; Jones, W., 2002, Karst Management Standards and Implementation Review, Final Report of the Karst Review Panel, Prepared for USDA Forest Service, Tongass National Forest, Submitted to MWH (Montgomery Watson Harza) under the terms of USDA Contract 53-0116-2-55901, 27 pp. and appendices.

Gutiérrez-Santolalla, F., Gutiérrez-Elorza, M., Marín, C., Desir, G., and Maldonado, C., 2005, Spatial distribution, morphometry and activity of La Puebla de Alfindén sinkhole field in the Ebro river valley (NE Spain): applied aspects for hazard zonation: Environmental Geology, v. 48, p. 360–369, doi: 10.1007/s00254-005-1280-8.

Harris, A.G., "Impacts of Forest Management and Timber Harvest Practices on Karst Critical Zone Processes in Tongass National Forest, Alaska", 2020, Masters Theses & Specialist Projects. Paper 3470.

Harris, A. S., Hutchinson, O. K., Meehan, W. R., Swanston, D. N., Helmers, A. E., Hindee, J. C., & Collins, T. M., 1974, 1. The Setting. In *The Forest ecosystem of southeast Alaska*. Portland, OR: Pacific Northwest Forest and Range Experiment Station.

Hendrickson, Melissa, "The Influence of Organic Acid on Limestone Dissolution: Tongass National Forest, Alaska", 2006, Masters Theses & Specialist Projects. Paper 3426. https://digitalcommons.wku.edu/theses/3426

Hendrickson, M.R., and Groves, C., 2011, From sink to resurgence: the buffering capacity of a cave system in the Tongass national forest, USA: Acta Carsologica, v. 40, doi: 10.3986/ac.v40i2.23.

Kienholz, C., Herreid, S., Rich, J.L., Arendt, A.A., Hock, R., and Burgess, E.W., 2015, Derivation and analysis of a complete modern-date glacier inventory for Alaska and northwest Canada: Journal of Glaciology, v. 61, p. 403–420, doi: 10.3189/2015jog14j230.

Kobal, M., Bertoncelj, I., Pirotti, F., Dakskobler, I., and Kutnar, L., 2015, Using Lidar Data to Analyse Sinkhole Characteristics Relevant for Understory Vegetation under Forest Cover—Case Study of a High Karst Area in the Dinaric Mountains: Plos One, v. 10, doi: 10.1371/journal.pone.0122070.

Koehler, R., and Carver, G., 2018, Active faults and seismic hazards in Alaska: doi: 10.14509/29705.

Köppen, W., 1984, The thermal zones of the EARTH according to the duration of hot, moderate and cold periods and to the impact of heat on the organic world. *Meteorologische Zeitschrift, 20*(3), 351-360. doi:10.1127/0941-2948/2011/105

Kovarik, J., 2007, Storm Response and Water Balance of Temperate Rainforest Karst Watersheds: Tongass National Forest, Alaska. Master's Thesis, Western Kentucky University, 78 p.

Kovarik, J., 2013, CAVE AND KARST RESOURCES AND MANAGEMENT IN THE UNITED STATES FOREST SERVICE. In 16th INTERNATIONAL CONGRESS OF SPELEOLOGY (p. 246).

Kovarik, J.L., 2013, Geologic management of cave and karst resources on national forest system lands; Proceedings of the 20th National Cave and Karst Management Symposium, November 4 through 8, 2013, Carlsbad, New Mexico ; Edited by: Lewis Land and Mark Joop, pp. 135-148

Kovarik, Johanna and James Baichtal, 2016, Contributions of Cave And Karst Research To Management On The Tongass National Forest, GSA Annual Meeting in Denver, Colorado, USA – 2016, DOI: 10.1130/abs/2016AM-284757

Kovarik, J., Baichtal, J., Prussian, K, and C. Ranger, 2005, Watershed Delineation in Karst Areas of the Tongass National Forest, Southeastern Alaska. Abstract, 14th International Congress of Speleology, Athens, Greece.

Langendoen, R.R. and Baichtal, J.F., 2004, November. Using LIDAR remote sensing to map karst topography in a temperate rain forest–Case study: Tongass National Forest, southeastern Alaska. In Geological Society of America Abstracts (p. 385).

Li, S., R.A. MacMillan, D.A. Lobb, B.G. McConkey, A. Moulin, and W.R. Fraser, 2011, "Lidar DEM Error Analyses and Topographic Depression Identification in Hummocky Landscape in the Prairie Region of Canada." Geomorphology 129: 263–75.

Lindsay, J.B., and Creed, I.F., 2006, Distinguishing actual and artefact depressions in digital elevation data: Computers & Geosciences, v. 32, p. 1192–1204, doi: 10.1016/j.cageo.2005.11.002.

Liu, H., and K.C., Jezek. 1999, "Investigating DEM Error Patterns by Directional Variograms and Fourier Analysis." Geographical Analysis 31: 249–66.

Maguire, D. J., 1991, Geographical information systems: Principles and applications. In *Geographical information systems: Principles and applications* (pp. 9-19). Essex, UK: Longman Scientific & Technical, 1991. v. 2. doi:http://lidecc.cs.uns.edu.ar/~nbb/ccm/downloads/Literatura/OVERVIEW%20 AND%20DEFINITION%20OF%20GIS.pdf

McClellan, M.H., Brock, T. and Baichtal, J.F., 2003, Calcareous fens in southeast Alaska. Res. Note PNW-RN-536. Portland, OR: US Department of Agriculture, Forest Service, Pacific Northwest Research Station, 536. https://www.fs.fed.us/pnw/pubs/pnw_rn536.pdf

Oksanen, J., 2003, *TRACING THE GROSS ERRORS OF DEM - VISUALIZATIONTECHNIQUES FOR PRELIMINARY QUALITY ANALYSIS*. Proceedings of the 21st International Cartographic Conference (ICC). Retrieved January 2, 2021. doi:https://icaci.org/files/documents/ICC_proceedings/ICC2003/Papers/288.pdf

Palmer, A.N., 2007, Cave geology: Dayton, OH, Cave Books.

Pecha, M.E., Gehrels, G.E., McClelland, W.C., Giesler, D., White, C. and Yokelson, I., 2016, Detrital zircon U-Pb geochronology and Hf isotope geochemistry of the

49

Yukon-Tanana terrane, Coast Mountains, southeast Alaska. Geosphere, 12(5), pp.1556-1574.

Prussian, K. and Baichtal, J., 2004, Delineation of a karst watershed on Prince of Wales Island, Southeast Alaska. In Advancing the fundamental sciences: Proc. For. Ser. Natl. Earth Sci. Conf. M. Furniss, C. Clifton, and R. Ronnenberg (editors) (pp. 111-117). http://citeseerx.ist.psu.edu/viewdoc/download?doi=10.1.1.156.2278&rep=rep1&type=pdf#page=129

Šegina, E., Benac, Č., Rubinić, J., and Knez, M., 2018, Morphometric analyses of dolines — the problem of delineation and calculation of basic parameters: Acta Carsologica, v. 47, doi: 10.3986/ac.v47i1.4941.

Sener, M., and Ozturk, M., 2019, Relict drainage effects on distribution and morphometry of karst depressions: a case study from central Taurus (Turkey): Journal of Cave and Karst Studies, v. 81, p. 33–43, doi: 10.4311/2018es0111.

Soja, C.M., 1990, Island Arc Carbonates from the Silurian Heceta Formation of Southeastern Alaska (Alexander Terrane): SEPM Journal of Sedimentary Research, v. Vol. 60, doi: 10.1306/212f9160-2b24-11d7-8648000102c1865d.

Soja, C.M., 1993, Carbonate Platform Evolution in a Silurian Oceanic Island: A Case Study from Alaska's Alexander Terrane: SEPM Journal of Sedimentary Research, v. Vol. 63, doi: 10.1306/d4267ca3-2b26-11d7-8648000102c1865d.

Soja, C.M., 2008, Silurian-bearing terranes of Alaska: The Terrane Puzzle: New Perspectives on Paleontology and Stratigraphy from the North American Cordillera, doi: 10.1130/2008.442(02).

Theilen-Willige, B., Malek, H., Charif, A., Bchari, F.E., and Chaïbi, M., 2014, Remote Sensing and GIS Contribution to the Investigation of Karst Landscapes in NW-Morocco: Geosciences, v. 4, p. 50–72, doi: 10.3390/geosciences4020050.

Veress Márton, Gutak, J.M., Lóczy Dénes, Ruban, D.A., Tóth Gábor, and Telbisz Tamás, 2019, Glaciokarsts: Cham, Springer.

Wang, L., & Liu, H., 2006, An efficient method for identifying and filling surface depressions in digital elevation models for hydrologic analysis and modelling. *International Journal of Geographical Information Science, 20*(2), 193-213. doi:10.1080/13658810500433453

Weishampel, J., Hightower, J., Chase, A., Chase, D., & Patrick, R., 2011, Detection and Morphologic analysis of Potential below-canopy Cave openings in the Karst landscape around the Maya polity of caracol using airborne Lidar. *Journal of Cave and Karst Studies, 73*(3), 187-196. doi:10.4311/2010ex0179r1

White, W. B., 1988, *Geomorphology and Hydrology of Karst Terrains*. Oxford University Press.

White, W.B., 2007, Evolution and Age Relations of Karst Landscapes: Acta Carsologica, v. 36, doi: 10.3986/ac.v36i1.207.

Williams, P.W., 1972, Morphometric Analysis of Polygonal Karst in New Guinea: Geological Society of America Bulletin, v. 83, p. 761, doi: 10.1130/0016-7606(1972)83[761:maopki]2.0.co;2.

Williams, P., 2008, The role of the epikarst in karst and cave hydrogeology: A review. *International Journal of Speleology, 37*(1), 1-10. doi:10.5038/1827-806x.37.1.1

WISSMAR, R., SWANSTON, D., BRYANT, M. and McGEE, K.A.T.H.E.R.I.N.E., 1997, Factors influencing stream chemistry in catchments on Prince of Wales Island, Alaska. Freshwater Biology, 38(2), pp.301-314.

Wu, Q., Deng, C., and Chen, Z., 2016, Automated delineation of karst sinkholes from LiDAR-derived digital elevation models: Geomorphology, v. 266, doi: http://dx.doi.org/10.1016/j.geomorph.2016.05.006.

Wu, Q., Lane, C.R., Wang, L., Vanderhoof, M.K., Christiansen, J.R., and Liu, H., 2019, Efficient Delineation of Nested Depression Hierarchy in Digital Elevation Models for Hydrological Analysis Using Level-Set Method: JOURNAL OF THE AMERICAN WATER RESOURCES ASSOCIATION, v. 55.

Zumpano, V., Pisano, L., and Parise, M., 2019, An integrated framework to identify and analyze karst sinkholes: Geomorphology, v. 332, p. 213–225, doi: 10.1016/j.geomorph.2019.02.013.

Fort Hays State University
FHSU Scholars Repository
Non-Exclusive License Author Agreement

I hereby grant Fort Hays State University an irrevocable, non-exclusive, perpetual license to include my thesis ("the Thesis") in *FHSU Scholars Repository*, FHSU's institutional repository ("the Repository").

I hold the copyright to this document and agree to permit this document to be posted in the Repository, and made available to the public in any format in perpetuity.

I warrant that the posting of the Thesis does not infringe any copyright, nor violate any proprietary rights, nor contains any libelous matter, nor invade the privacy of any person or third party, nor otherwise violate FHSU Scholars Repository policies.

I agree that Fort Hays State University may translate the Thesis to any medium or format for the purpose of preservation and access. In addition, I agree that Fort Hays State University may keep more than one copy of the Thesis for purposes of security, back-up, and preservation.

I agree that authorized readers of the Thesis have the right to use the Thesis for non-commercial, academic purposes, as defined by the "fair use" doctrine of U.S. copyright law, so long as all attributions and copyright statements are retained.

To the fullest extent permitted by law, both during and after the term of this Agreement, I agree to indemnify, defend, and hold harmless Fort Hays State University and its directors, officers, faculty, employees, affiliates, and agents, past or present, against all losses, claims, demands, actions, causes of action, suits, liabilities, damages, expenses, fees and costs (including but not limited to reasonable attorney's fees) arising out of or relating to any actual or alleged misrepresentation or breach of any warranty contained in this Agreement, or any infringement of the Thesis on any third party's patent, trademark, copyright or trade secret.

I understand that once deposited in the Repository, the Thesis may not be removed.

Thesis: _A KARST FEATURE PREDICTION MODEL FOR PRINCE OF WALES ISLAND, ALASKA BASED ON HIGH RESOLUTION LiDAR IMAGERY_

Author: _Alexander S. Lyles_

Signature: _Alex Lyle_

Date: _5/3/2021_